




Insights into the selective sensing mechanism of a luminescent Cd(II)-based MOF chemosensor toward NACs: roles of the host–guest interactions and PET processes

Yoan Hidalgo-Rosa^{1,5}, Karel Mena-Ulecia^{2,7}, Manuel A. Treto-Suárez³, Eduardo Schott^{3,5}, Dayán Páez-Hernández^{1,6,*} , and Ximena Zarate^{4,*}

¹ Doctorado en Físicoquímica Molecular, Universidad Andres Bello, Ave. República #275, Santiago, Chile

² Departamento de Ciencias Biológicas Y Químicas, Facultad de Recursos Naturales, Universidad Católica de Temuco, Ave. Rudecindo Ortega 02950, Temuco, Chile

³ Departamento de Química Inorgánica, Facultad de Química y de Farmacia, Centro de Energía UC, Centro de Investigación en Nanotecnología Y Materiales Avanzados CIEN-UC, Pontificia Universidad Católica de Chile, Vicuña Mackenna 4860, Macul, Santiago, Chile

⁴ Facultad de Ingeniería, Instituto de Ciencias Químicas Aplicadas, Universidad Autónoma de Chile, Av. Pedro de Valdivia 425, Santiago, Chile

⁵ ANID – Millennium Science Initiative Program- Millennium Nuclei on Catalytic Process towards Sustainable Chemistry (CSC), Santiago, Chile

⁶ Center of Applied Nanosciences (CANS), Universidad Andres Bello, República #330, Santiago de Chile, Chile

⁷ Núcleo de Investigación en Bioproductos Y Materiales Avanzados (BIOMA), Facultad de Ingeniería, Universidad Católica de Temuco, Ave. Rudecindo Ortega 02950, Temuco, Chile

Received: 29 March 2021

Accepted: 14 May 2021

Published online:
24 May 2021

© The Author(s), under exclusive licence to Springer Science+Business Media, LLC, part of Springer Nature 2021

ABSTRACT

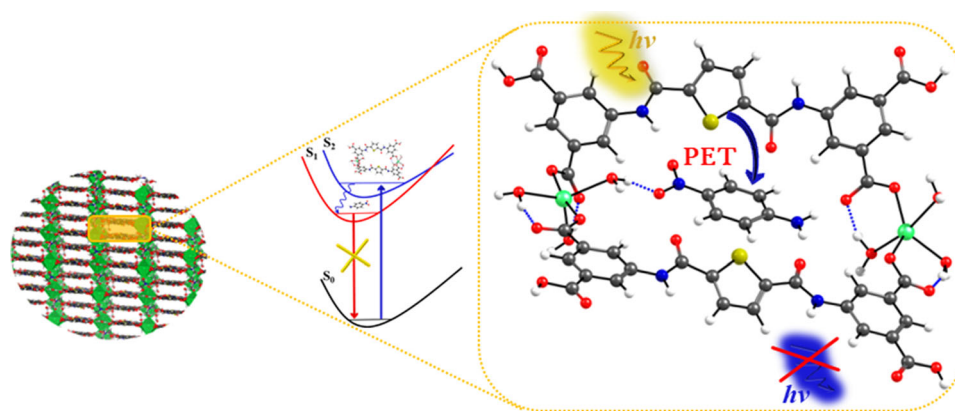
The structural and photophysical properties of the $[\text{Cd}_2(\text{H}_4\text{L})_2(\text{H}_2\text{O})_5] \cdot 5\text{H}_2\text{O}$ (where H_4L is the ligand 5,5'-((thiophene-2,5-dicarbonyl)bis(azanediyl))di-isophthalic acid labeled as Cd-MOF), as well as the elucidation of the selective *turn-off* luminescent sensing mechanism toward 4-nitroaniline (pNA) were addressed, using quantum chemical methods. To reach this aim, the structures of the ground state (S_0) and first excited state (S_1) Cd-MOF/analyte system were assessed. We found that after the interaction a photoinduced electron transfer (PET) from the Cd-MOF to pNA is responsible for the fluorescence quenching in this system. For this purpose, a study was performed based on TD-DFT and multireference calculations to corroborate that an excited state exists with the adequate electronic configuration for PET process in the interacting system Cd-MOF/analyte. Intermolecular interaction between the Cd-MOF and analyte was studied by means of Morokuma–Ziegler energy decomposition analysis, natural

Handling Editor: Pedro Camargo.

Address correspondence to E-mail: dayan.paez@unab.cl; ximena.zarate@uautonoma.cl

orbitals of chemical valence, *ab initio* molecular dynamics (AIMD) calculations and non-covalent interactions (NCI) index. These results showed that intermolecular interactions via hydrogen bond are considerably strengthened in the excited state for the Cd-MOF/pNA, which favor the non-radiative deactivation channels of the chemosensor. In addition, the overlap of absorption spectra of Cd-MOF and pNA indicates that the loss of fluorescence is also due to internal filter effect (IFE). The most noteworthy aspect of this methodology is to consider the relative energies of the S_0 and S_1 states of MOF/analyte system to explaining the experimental behavior of Cd-MOF toward 4-nitroaniline, proving to be a robust tool in the accurate elucidation of the sensing mechanism in the MOF chemosensor.

GRAPHICAL ABSTRACT



Ab initio methods along with TD-DFT have been used to elucidate the selective turn-off luminescent sensing mechanism of nitroaromatic compounds by a Cd-based metal–organic framework (MOF). The role of the host–guest interaction has been pointed out using different theoretical descriptors. A theoretical protocol is given to get more insights into the MOF design and selectivity for nitroaromatic compounds.

Introduction

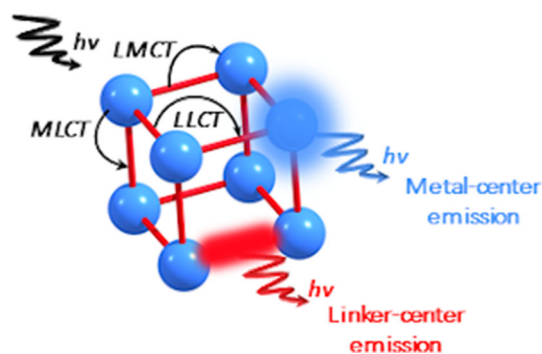
Chemical detection of nitroaromatic compounds (NACs) has acquired a special relevance in recent years. The growing interest in the sensing of NACs is mainly due to their adverse impacts on the environment and human health. On the one hand, some of these compounds have been classified as toxic or carcinogenic compounds [1, 2], while others with high explosive power are used in the manufacture of improvised explosive devices that represent a potential risk in terms of security [3, 4]. Besides, NACs are considered hazardous pollutants, mainly

due to presence in the environment by their extensive use in many industrial processes, such as agro-chemical, dyes, explosives, among others [5, 6]. This is one of the reasons that NACs are found in the environment in risky concentrations to health and ecosystems [7, 8]. In this regard, chemical sensors, besides of providing information *in situ* about the detection of chemical species, have certain advantages in terms of rapid response time, accuracy, reliability and low cost [9, 10]. This fact has led luminescent metal–organic frameworks (L-MOFs) as successful alternatives to develop chemosensors based on the luminescence changes upon recognition of the analytes [11, 12]. Among these chemosensors,

luminescent systems have currently encouraged researchers to focus on designing materials that show a remarkable response in their optical properties, induced by the host–guest interactions with a specific analyte (guest) [13, 14]. L-MOFs have interesting structural features that are responsible of special luminescent properties, since light emission in L-MOFs generally arises from their building components: linkers (conjugated organic ligands) and/or nodes (metal ions or clusters). The linkers are coordinated to the ions from the nodes in a rigid coordination network, which causes the components to be almost immobilized in the structure, with an ordered orientation. This restricts at least to some degree, rotation, or vibration modes of the structure. The luminescent properties of the L-MOFs are described by different mechanisms such as ligand-to-ligand charge transfer (LLCT), ligand-to-metal charge transfer (LMCT), metal-to-ligand charge transfer (MLCT), metal-centered emission and ligand-centered emission, see Scheme 1 [15, 16].

In these systems, the chemical sensing is based on the change in the emission intensity, either the enhancement or quenching of the luminescence upon the interaction of the analyte with the L-MOF. According to these feasible responses, the chemosensor is called “turn-off” when luminescence quenching occurs, while a sensor with a “turn-on” response involves a luminescence activation or enhancement upon the interaction of the sensor with the analytes [17, 18]. Both types of chemosensors are illustrated in Scheme 2.

More recent research has employed theoretical approaches thorough computational simulations to

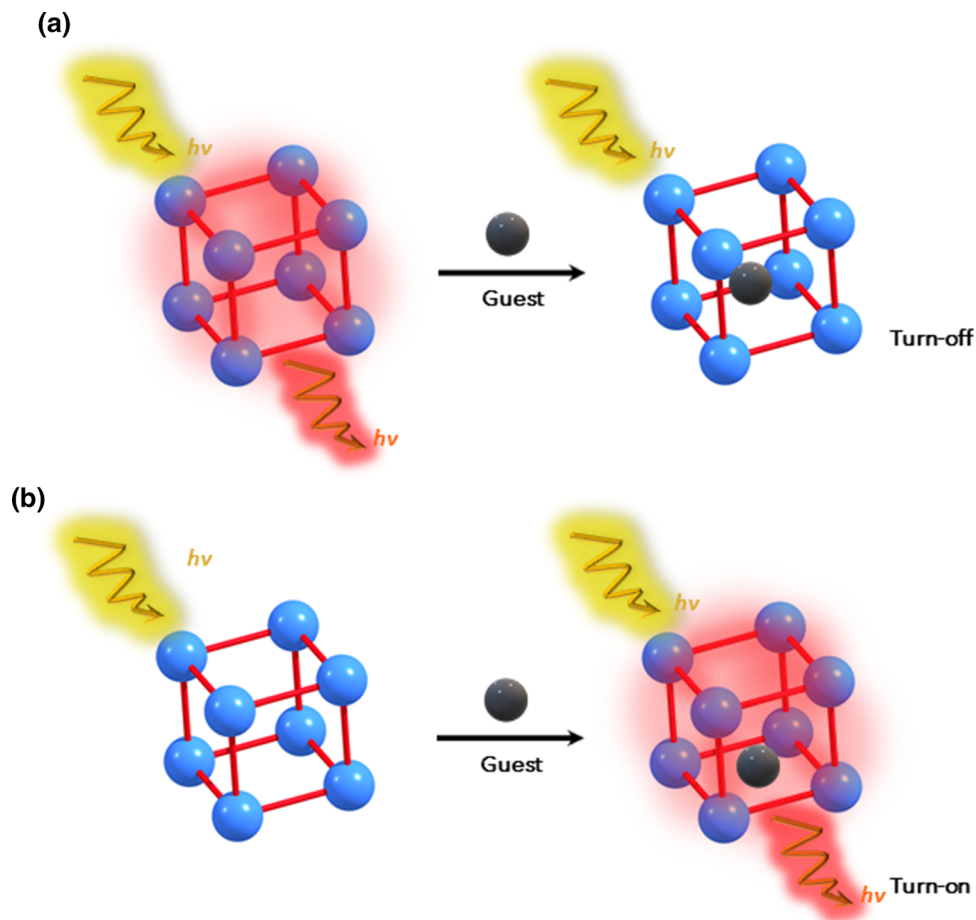


Scheme 1 Schematic representation of possible photophysical processes from L-MOFs, where blue balls represent the nodes (metal ions or metal clusters) and the red sticks represent linkers (organic ligands).

elucidate the detection principle in L-MOF-based chemosensors, as it is reported in a review by Jian-Qiang Liu et al. [19]. Nevertheless, the enhancement or quenching of luminescence has not been fully studied taking into account the interaction of L-MOF with the analyte as a whole interacting system. For example, many previous reports have discussed that the energy value of the LUMO of the analytes such as NACs should be located between the conduction band (CB) and valence band (VB) of the sensor. This is to explain the photoinduced electron transfer (PET) process that governs the observable property in terms of the luminescent change from the sensor [20, 21]. Besides, it should also be noted, as mentioned earlier, that the sensing process implied a change in the emission properties of the chemosensor upon the incorporation of the analyte. Thus, it is crucial to have a precise description of electronic states involved in the optical properties of the host–guest system. In this sense, it is worthy to mention that host–guest systems have also attracted great attention for other recently reported applications of MOFs, such as the biomedical field (*e.g.*, the development of drug carriers [22], biosensors [23], among others). So, considering that the computational simulations have been helpful tools to provide detailed description and interpretation of the capture and selective interaction of target molecules by MOFs, several approaches have been explored. For example, the Grand canonical Monte Carlo simulations have been used to study the adsorption of small molecules [24], the semi-empirical extended Hückel method was used to describe the electronic densities of states (DOS) [25], or the analysis of the host–guest interaction was performed via energy decomposition analysis (EDA) and non-covalent interaction (NCI) analysis [14, 26]. Finally, to the best of our knowledge, the available theoretical works have not yet clarified the responsible phenomena of the L-MOFs chemosensors selectivity toward NACs considering the energies of the excited states. In this sense, the photoluminescence emission (fluorescence or phosphorescence) occurs from the lowest excited state of a given multiplicity, according to Kasha’s rule [27]. Regarding this, it should be considered the relative energies and structures of the first excited states (S_1 or T_1), to explain in detail the sensing mechanism of the chemosensor luminescence [28, 29]. In consequence, we consider that there is a lack of rigorous theoretical studies of these processes, not only in the sense of elucidating the feasible

Scheme 2 Schematic representation.

a Luminescence turn-off type chemosensor; **b** Luminescence turn-on type chemosensor, where blue balls represent the nodes (metal ions or metal clusters), the red sticks represent linkers (organic ligands) and black ball represents a “guest” which is an analyte.



pathways of activation/deactivation of luminescence but also for the design and synthesis of novel chemosensors with suitable properties for sensing analytes of interest.

Having all these facts in mind, here we propose a computational procedure using density functional theory (DFT) and time-dependent DFT (TD-DFT) approaches, which successfully allowed to understand the sensing mechanism of Cd-based MOF, i.e., $[\text{Cd}_2((\text{H}_2\text{L})_2(\text{H}_2\text{O})_5)]0.5\text{H}_2\text{O}$ where H_4L corresponds to the ligand 5,5'-((thiophene-2,5-dicarbonyl)bis(azanediyl)) diisophthalic acid, reported by Fengqin Wang et al. [30] in 2017, selective to 4-nitroaniline (pNA). In detail, this sensor exhibits high selectivity to pNA, compared to the other nitro compounds, through a *turn-off* fluorescence response. Also, we have studied Cd-MOF/analyte systems using the Morokuma–Ziegler energy decomposition scheme (EDA) and the natural orbital of chemical valence (NOCV). These results along with the evidence of most sophisticated analyses such as, *ab initio* molecular dynamics (AIMD) calculations and non-

covalent interactions (NCI) index, supplied deeply insights of the nature of host–guest interactions and their role on the sensing response of the studied MOF. Furthermore, we addressed the elucidation of changes that govern the sensing mechanism of the chemosensor based on relative energies of the ground and the first excited states, as well as from the interacting system Cd-MOF/analyte. Our theoretical approach provided a basis for elucidating the selective NACs detection mechanism by L-MOFs, by means of an accurate description of interactions of the chemosensor with the analytes and the excited states energies of the Cd-MOF and Cd-MOF/analyte systems.

Computational details

The theoretical study of a MOF-based system via electronic structure calculations is a particular challenge due to the large size of this system. From the computational point of view, a very useful reported

alternative is to truncate an extended structure to a finite fragment, which represents the structure of interest [26, 31]. In the herein study, the structural model proposed consists of the representative fragment $[\text{Cd}_2(\text{H}_2\text{L})_2(\text{H}_2\text{O})_6]$, H_4L : 5,5'-((thiophene-2,5-dicarbonyl)bis(azanediyl))diisophthalic acid, designed starting from the reported structure of the extended system, which we will refer as Cd-MOF, see Fig. 1.

In this study, the analytes were chosen based on fluorescence quenching efficiency of the Cd-MOF as previously reported by Fengqin Wang et al. [30], *i.e.*, pNA, highest quenching effect, nitrobenzene (NB), smaller quenching effect; and nitromethane (NM) which shows non-quenching of the luminescence of the Cd-MOF.

As first stage in this study, geometry optimizations of the Cd-MOF and Cd-MOF/analyte systems were carried out in the framework of the Density Functional Theory (DFT) approach, with the hybrid exchange and correlation Becke-three-parameter Lee–Yang–Parr (B3LYP) functional [32, 33], using ORCA 4.4 program package [34]. Further, the basis set, triple- ζ valence with two sets of polarization functions, def2-TZVPP [35], was used for the C, H, N, O and S atoms. Taking into account that the Cd atom does not present a marked relativistic effect, the Stuttgart–Dresden-type effective core potential (ECP) to treat scalar effects was incorporated [37]. All calculations were performed using the SDD pseudopotential for

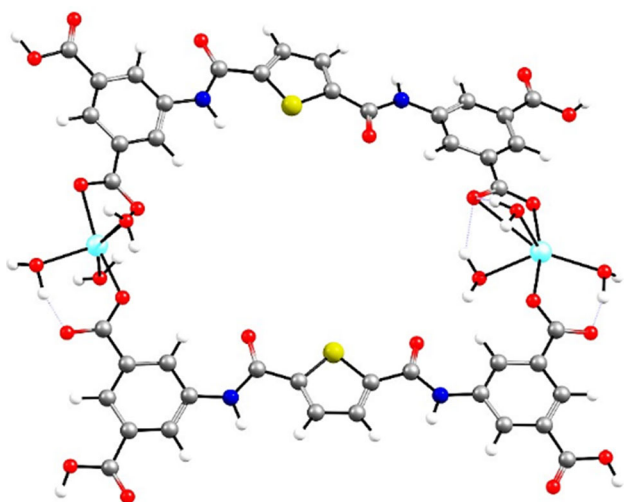


Figure 1 Optimized geometry of the structural model $[\text{Cd}_2(\text{H}_2\text{L})_2(\text{H}_2\text{O})_6]$ at B3LYP/TZ2P theoretical level. Atoms: Gray: C, white: H, blue: N, red: O, cyan: Cd and yellow: S.

Cd that replaces 28 core electrons and while the outer electrons are treated with def2-TZVPP basis set. The solvation effects were considered via a conductor-like screening model (CPCM) using the parameters of 2-propanol as solvent (dielectric constant, $\epsilon = 18.23$ and refraction index = 1.377) [36].

The charge distributions of the Cd-MOF/analyte systems were visualized through the method of molecular electrostatic potential (MEP) of the molecular surface. This approach allows us a three-dimensional visualization of the distribution of the electrostatic potential (electrons + nuclei) of the system, which is based on the electronic density function of the system given by Eq. 1 [37, 38]:

$$V(r) = \sum_A \frac{Z_A}{|\mathbf{R}_A - \vec{r}|} - \int \frac{\rho(\vec{r}') d\mathbf{r}'}{|\vec{r} - \vec{r}'|} \quad (1)$$

where $V(r)$ is defined in terms of the electronic density function of the molecule $\rho(r')$, and the charge of the nucleus A (Z_A), located in \mathbf{R}_A .

To perform the analysis of the host–guest interactions, the Cd-MOF/analyte systems were optimized in their ground (S_0) and the first singlet excited (S_1) states. In the first step, the host–guest interactions were analyzed through energy decomposition analysis (EDA) proposed by Morokuma–Ziegler scheme [39, 40]. This analysis was carried out using the Amsterdam Density Functional (ADF) package [41]. The systems were divided into two fragments, *i.e.*, Cd-MOF and analyte, where analyte is 4-nitroaniline (pNA), nitrobenzene (NB) or nitromethane (NM), according to fragmentation scheme of the EDA analysis. The interaction energy (ΔE_{int}) between the two fragments decomposes into four terms, as indicated in Eq. 2.

$$\Delta E_{\text{int}} = \Delta E_{\text{Pauli}} + \Delta E_{\text{Elec}} + \Delta E_{\text{Orb}} + \Delta E_{\text{Disp}}. \quad (2)$$

Here, ΔE_{Pauli} describes the repulsive interaction of Pauli, between occupied orbitals of both molecular fragments. The second term ΔE_{Elec} refers to the classical electrostatic interaction between both fragments. The third term ΔE_{Orb} accounts for possible interactions between molecular orbitals (MOs) related to the charge transfer, polarization, etc. This term can be analyzed by the natural orbital of chemical valence (NOCV) method proposed by Mitoraj [42]. The term ΔE_{Disp} is related to dispersion forces acting between the fragments, which was incorporated with Grimme's D3 dispersion correction for EDA

calculations [43]. For all systems, the interaction energies between Cd-MOF and analyte were corrected via the counterpoise method to the basis set superposition error (BSSE) [44]. In addition, the interaction between the Cd-MOF and the NACs was also investigated through the non-covalent interaction (NCI) approach [45, 46]. The optimized structures of the S_0 and S_1 states of the system were the input data to calculate the non-covalent interaction (NCI) index. The NCI analysis was performed employing Multiwfn [47] and NCIPLOT programs [45]; the scripts used to automate the analysis of NCI index as well as the visualization and creation of the corresponding images were carried out through the VMD program [48, 49].

The optical properties of the (absorption and emission) of the Cd-MOF and Cd-MOF/analyte systems were calculated using time-dependent density functional theory (TD-DFT), with the B3LYP functional and the same basis set employed in the geometry optimizations [50, 51].

Fluorescence rate constant k_F is determined through the simplified version of the Strickler–Berg equation (3) [52, 53]:

$$k_{F,SB} = 4.34 * 10^7 [s^{-1}eV^{-2}] \frac{E_{F,vert}^3}{E_{A,vert}} f \quad (3)$$

where $E_{F,vert}$, and $E_{A,vert}$ are the energies of vertical excitations Franck–Condon, computed through TD-DFT, for the emission and absorption, respectively, and f is the oscillator strength of the emitting state.

To analyze the existence of an excited state with the appropriate electronic configuration for the PET from the Cd-MOF to the NACs (*i.e.*, pNA or NB) mechanism, the complete active space self-consistent field (CASSCF) method was used [54]. The dynamical correlation was also included through n -electron valence state perturbation theory (NEVPT2) approach [55], to correct energies of CASSCF calculations. Active space of ten electrons in ten orbitals was used to obtain the energy values of the S_0 , S_1 and T_1 states.

The final step was to analyze the behavior of the intermolecular hydrogen bonds (HB) over time, for the Cd-MOF/NACs system. These interactions were simulated through the ab initio molecular dynamics (AIMD) method [56, 57]. For each system, 100 fs of simulation time with 0.5 fs of time step at 298.15 K was performed. All ab initio MD simulations were carried out using the ORCA 4.4 program package [34]

and trajectory analyses were computed using VMD program [48, 49].

Results and discussion

Molecular geometry

The optimization of the ground state geometries of all systems, in general, showed a good correlation with the experimental values. In all four systems, Cd-MOF and Cd-MOF/analyte (analyte: pNA, NB and NM), the computed bonds lengths Cd–O around the cadmium atom are in the range from 2.219 Å to 2.501 Å, being the experimental values for Cd-MOF, between 2.263 Å and 2.474 Å [30]. These results suggest that the structural models proposed are effective for the performance of the theoretical approach at this level of theory. An interacting model as starting structures to simulate the Cd-MOF/analyte interaction was considered for each analyte. The interaction occurs between the aromatic ring of the linker and the analyte. The final conformations of the ground state Cd-MOF/analytes systems consisted of the analyte, *i.e.*, pNA, NB, or NM, confined into the Cd-MOF. The results indicate intermolecular HB formation, between an aqua ligand coordinated to the Cd^{2+} ion and nitro ($-NO_2$) of analytes ($O \cdots H$), as well as with amino ($-NH_2$) groups ($H \cdots N$), in the case of pNA. These results agree with the experimental results reported by Fengqin Wang et al. [30] in 2017 for this chemosensor. They pointed out that the analytes are encapsulated into the Cd-MOF through HB interactions. The intermolecular H bonds lengths of the, ($O \cdots H$) and ($H \cdots N$), of the Cd-MOF/analyte system under study are summarized in Table 1 for the S_0 and

Table 1 Ground (S_0) and the first singlet excited (S_1) states HB lengths for Cd-MOF/analyte, distances (Å) at B3LYP/ def2-TZVPP

	HB	Cd-MOF/ pNA	Cd-MOF/ NB	Cd-MOF/ NM
S_0 state	($O \cdots H$)	1.867	1.904	2.033
	($H \cdots N$)	1.967	–	–
S_1 state	($O \cdots H$)	1.720	1.965	2.025
	($H \cdots N$)	2.804	–	–

($O \cdots H$) and ($H \cdots N$) are intermolecular hydrogen bonding (HB) between aqua ligand of Cd-MOF and which the nitro group ($-NO_2$) and ($-NH_2$) groups, respectively, of the analyte

S_1 states. For the Cd-MOF/pNA the intermolecular HB ($O\cdots H$) is shortened in the S_1 state, while in the case of Cd-MOF/NB, the intermolecular HB ($O\cdots H$) becomes slightly longer in the excited state. Nevertheless, the intermolecular HB ($O\cdots H$) for Cd-MOF/NM system remains almost unaltered in the S_1 state, compared to the S_0 state. All these HB interactions are illustrated in Fig. S1, Electronic Supplementary Material.

In this sense, in many previous works, it has been reported that the intermolecular HB strengthening in the excited state contributes to the non-radiative deactivations of the emissive state [58, 59]. It should be noted that the HB ($O\cdots H$) interaction length between Cd-MOF and pNA is shortened from 1.867 Å in the S_0 state to 1.720 Å in the S_1 state. Thus, it could be thought that as a consequence of this strengthening of HB interaction in the S_1 state, the optical behavior of interacting system Cd-MOF/pNA change. To get a deeper insight, we studied in detail the nature of the interaction between the Cd-MOF and analytes.

Host–guest interaction analysis

An analysis of molecular charge distributions can provide evidence about of intermolecular interactions in the host–guest system. In this sense, Politzer and Murray pointed out “it is through this potential that a molecule is first ‘seen’ or ‘felt’ by another approaching chemical species” [60]. From this perspective, the charge distributions in regions of intermolecular HBs interactions of the Cd-MOF with analyte through electrostatic potential maps analysis were explored. Figure 2a displays the gradient of charge distribution for Cd-MOF/pNA system where the intermolecular interactions of HBs are evidenced. It can be seen the

regions, where $V_s(r) > 0$ (green zone) is around the aqua ligands, and $V_s(r) < 0$, (red zone) are located near the ($-\text{NO}_2$) and ($-\text{NH}_2$) groups of the pNA. A similar result is illustrated in Fig. 2b for Cd-MOF/NB system; note that in the zone of approximation between the Cd-MOF and NB green iso-surfaces located on the hydrogen atoms of aqua ligand can be identified, while a red iso-surfaces are located over oxygen atoms of ($-\text{NO}_2$) group, for the HB ($O\cdots H$) interaction. The mapping of the electrostatic potential of the Cd-MOF/NM system indicates also similar features respect to the intermolecular HB ($O\cdots H$), see Fig. S2 in the Electronic Supplementary Material.

To gain a deeper understanding of these interactions both in the ground state and in the excited state, the analysis via the EDA scheme and the NOCV approach was performed. In all three studied cases, in the fragmentation scheme the Cd-MOF and analyte, *i.e.*, pNA, NB and NM, were employed as fragments. As it is shown in Table 2, in the ground state the host–guest interaction energies suggest that the interaction between Cd-MOF and pNA (analyte that turns-off the luminescence of the sensor) is stronger, $\Delta E_{\text{int}} = -30.45$ kcal/mol, than the interaction of Cd-MOF with NB and NM, $\Delta E_{\text{int}} = -18.68$ kcal/mol and $\Delta E_{\text{int}} = -12.96$ kcal/mol, respectively.

Furthermore, the electrostatic component is the most important stabilizing term for all three systems, both in the S_0 state and in the S_1 state. The results also revealed that the dispersive forces (*van der Waals*) that act between the Cd-MOF and analyte are relevant, specifically the dispersion component represented 20% of the total stabilizing energy in case of pNA, 32% for NB, and 22% for NM.

On the other hand, the calculations show stronger interaction energy for Cd-MOF/pNA system in the excited state S_1 (-35.66 kcal/mol) compared to the

Figure 2 Electrostatic potential maps computed at B3LYP/TZ2P level and isodensity value 0.003 a.u. of **a** Cd-MOF/pNA and **b** Cd-MOF/NB.

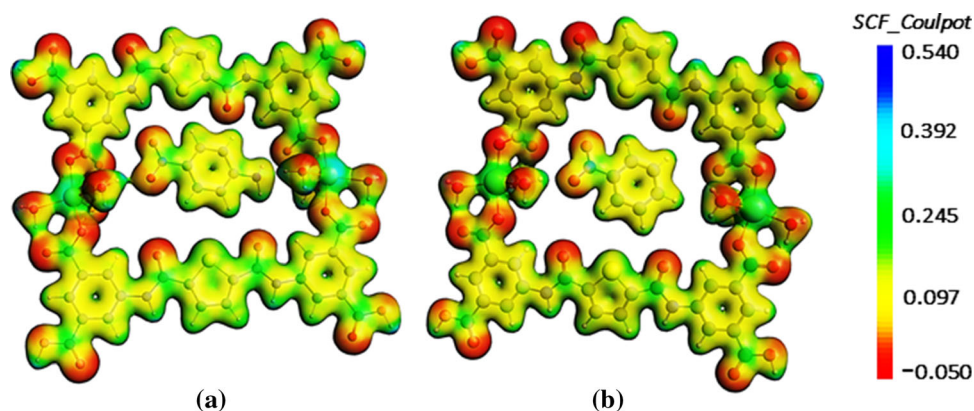


Table 2 Morokuma–Ziegler scheme energy decomposition analysis (EDA), values in kcal/mol, for the Cd-MOF/analyte interacting systems

System	ΔE_{Pauli}	$\Delta E_{\text{Elastat}}$	ΔE_{Orb}	ΔE_{Disp}	ΔE_{Int}
<i>S₀ state</i>					
Cd-MOF-pNA	27.19	− 29.90(51%)	− 17.19(29%)	− 11.86(20%)	− 30.45
Cd-MOF-NB	12.17	− 14.09(44%)	− 7.61(24%)	− 10.12(32%)	− 18.68
Cd-MOF-NM	7.53	− 11.60(55%)	− 4.88(23%)	− 4.58(22%)	− 12.96
<i>S₁ state</i>					
Cd-MOF-pNA	29.27	− 32.87(50%)	− 20.00(30%)	− 13.50(20%)	− 35.66
Cd-MOF-NB	9.67	− 12.97(43%)	− 7.17(24%)	− 9.70(33%)	− 19.10
Cd-MOF-NM	7.64	− 11.59(55%)	− 4.92(23%)	− 4.60(22%)	− 12.90

S_0 state (− 30.45 kcal/mol). This stabilization is expected due to the decrease in the HB (O⋯H) distance in the S_1 state. In case of Cd-MOF/NB system, interaction energy indicates that a slight change from the ΔE_{int} value for the S_1 state (− 19.10 kcal/mol) in comparison with ΔE_{int} (− 18.68 kcal/mol) in the S_0 state, while, for the Cd-MOF/NM system, the ΔE_{int} are close, being (− 12.96 kcal/mol) for the S_0 and (− 12.90 kcal/mol) for S_1 .

For both systems, Cd-MOF/NM and Cd-MOF/NB, the variations in the interaction energy between the S_0 state and the S_1 state are negligible and are in good agreement with the changes in the distances of the intermolecular HBs interaction, pointed in the above section.

To explore in detail channels of donor–acceptor interaction between Cd-MOF and the analytes, we performed an analysis based on the NOCV methodology proposed by Mariusz P. Mitoraj and Artur Michalak [42, 61]. For Cd-MOF/pNA system, the donor–acceptor interaction is due to intermolecular HB (H⋯N) and (O⋯H), formed between Cd-MOF and the pNA molecule. Furthermore, the calculations show that these interactions involved a donation of the lone pair of nitrogen (from $-\text{NH}_2$ group) and oxygen (from $-\text{NO}_2$ group) of the pNA molecule, to the hydrogen atom of a Cd-MOF aqua ligand. The deformation density analysis revealed that (H⋯N) interaction, $\Delta\rho_1$, is a more stabilizing contribution with $\Delta E_{\text{Orb}}(1) = -5.28$ kcal/mol compared to, $\Delta\rho_2$, $\Delta E_{\text{Orb}}(2) = -3.93$ kcal/mol for (O⋯H) interaction, for (a) and (b) in Fig. 3. It should be noted that the contribution in the ground state of the $\Delta E_{\text{Orb}}(1)$ (H⋯N) and $\Delta E_{\text{Orb}}(2)$ (O⋯H) interaction to the total orbital interaction (ΔE_{Orb}) is 31% and 23%, respectively.

NOCV analysis also indicated that the deformation density channel, $\Delta\rho_1$ which is originated

predominantly from the electron donation due to intermolecular HB (H⋯N), displays a redistribution of electron density localized along the pNA molecule, in the S_1 state, see Fig. 3c. This result is consistent with the lengthened of the intermolecular distance (H⋯N) in the excited state. In contrast, in the S_1 state, the $\Delta E_{\text{orb}}(2)$ indicate a stabilization of (O⋯H) interaction between Cd-MOF and pNA, see Fig. 3 (d). This result is consistent with the decrease in the (O⋯H) interaction distance in that state, as discussed in the previous section.

Figure S3 in the Electronic Supplementary Material illustrates the NOCV deformation density channels between NB and Cd-MOF. This donor–acceptor interaction involves the (O⋯H) interaction from a lone electron pair of an oxygen atom, of ($-\text{NO}_2$) group of the analyte and the hydrogen atom of a Cd-MOF aqua ligand. According to the orbital energy term this interaction is weaker in S_1 (− 2.6 kcal/mol) state than in S_0 (− 3.2 kcal/mol) state. These results agree with the intermolecular HB distance increase in the S_1 excited state for this system.

Finally, in case of the Cd-MOF/NM system, the deformation density channel displays an HB (O⋯H) interaction between the analyte and framework, see Fig. S4 in the Electronic Supplementary Material. Through this analysis, we identified that intermolecular HB is due to the interaction between the hydrogen atoms of the aqua ligand with the lone pairs of the O atoms, of the $-\text{NO}_2$ group. Furthermore, the deformation density channel, $\Delta\rho_1$ with $\Delta E_{\text{Orb}}(1) = -2.20$ kcal/mol for S_0 state showed similar features compared to $\Delta\rho_1$ channel with − 2.23 kcal/mol for (O⋯H) bonding interaction in the S_1 state.

The analysis of non-covalent interaction through the NCI index has made it possible to extend theoretical studies to distinguish weak interactions such

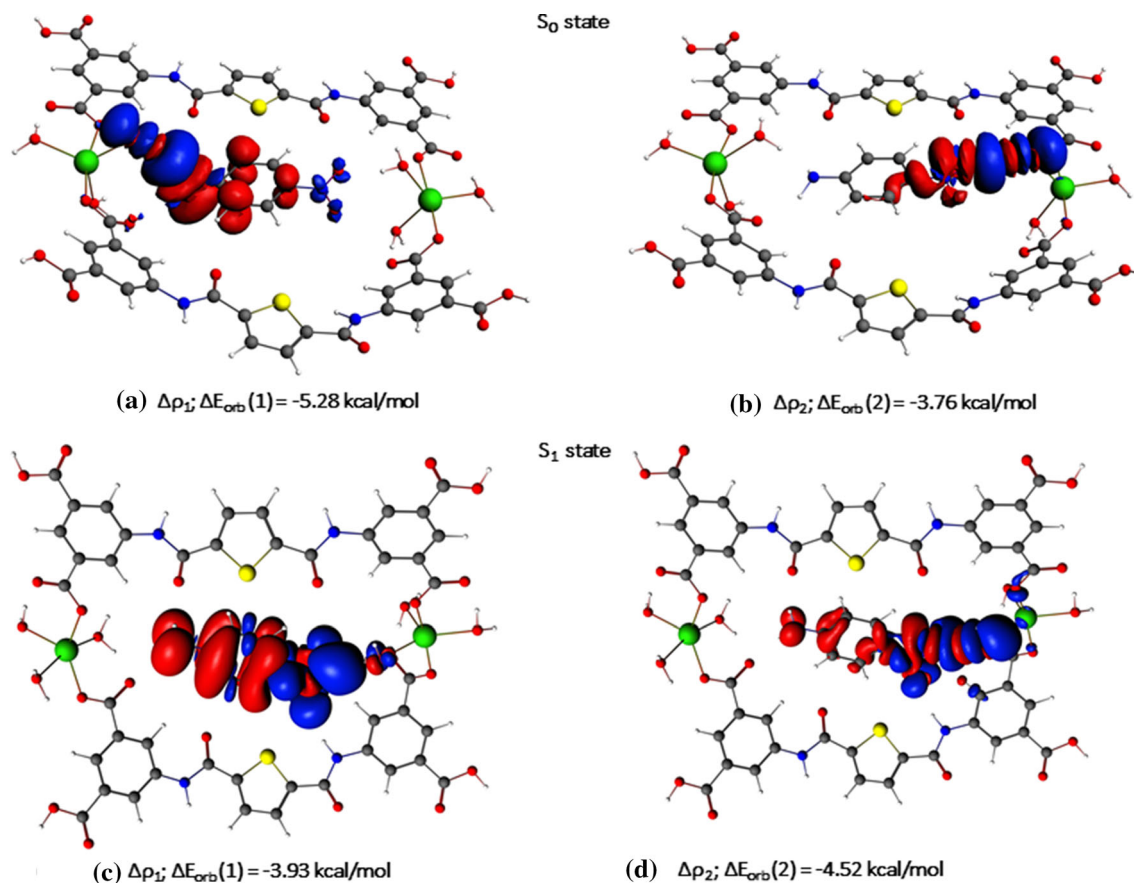


Figure 3 Contours of deformation density channels ($\Delta\rho$) with the corresponding energies, in kcal/mol, describing the intermolecular HB ($\text{H}\cdots\text{N}$) and ($\text{O}\cdots\text{H}$) interactions in Cd-MOF/pNA (a) and

(b) EDA-NOCV analysis of the ground state; c and d EDA-NOCV analysis of the S_1 excited state.

as hydrogen bonds, *van der Waals* interactions and repulsive steric interactions. Such approach allows distinguishing these interactions according to the second eigenvalue (λ_2) of the electron-density Hessian (second derivative) matrix, *e.g.*, attractive interactions $\text{sign}(\lambda_2)\rho > 0$, where hydrogen bonds appear at $(\text{sign}(\lambda_2)\rho < 0)$, while the *van der Waals* interactions at values $(\text{sign}(\lambda_2)\rho \approx 0)$ and repulsive interaction $\text{sign}(\lambda_2)\rho > 0$ [45, 46]. To go deeper on the intermolecular HBs between the Cd-MOF and the NACs, this interaction was analyzed through the NCI index, for both the S_0 state and the S_1 state. As can be seen in Fig. 4a, in the plot of reduced density gradients (RDGs) versus $\text{sign}(\lambda_2)\rho$ for the geometry of the S_0 state of the Cd-MOF/pNA system, a peak at around of -0.030 a.u. appears, which corresponds to the HBs interactions. However, for the excited state, where the length of the intermolecular HB ($\text{O}\cdots\text{H}$) between the Cd-MOF and pNA is shorter than in the S_0 , this peak appears at -0.040 a.u., clearly shifted

concerning the HB interaction in the S_0 state, see Fig. 4b. Conversely, for the Cd-MOF/NB system can be distinguished a slight shift of the peak that appears in the HB region, from -0.025 a.u. to near 0.020 a.u. for the simulated host-guest interaction in the S_0 state and S_1 state, respectively, see Fig. S5 in the Electronic Supplementary Material. Together, these results indicate a lengthening of the intermolecular interaction ($\text{O}\cdots\text{H}$) from Cd-MOF/NB in the S_1 state, as already mentioned above. Overall, these results are in good agreement with the analysis via EDA and the NOCV described in the previous section, where it is shown that the intermolecular HB ($\text{O}\cdots\text{H}$) is stronger ($\Delta E_{\text{orb}}(2) = -4.52$ kcal/mol) in the S_1 state as compared to $\Delta E_{\text{orb}}(2) = -3.76$ kcal/mol in the S_0 state, due to enhancement of donor-acceptor interaction.

Finally, it is worthy to highlight that our results provide strong evidence of the intermolecular HB strengthening between Cd-MOF and pNA in the S_1

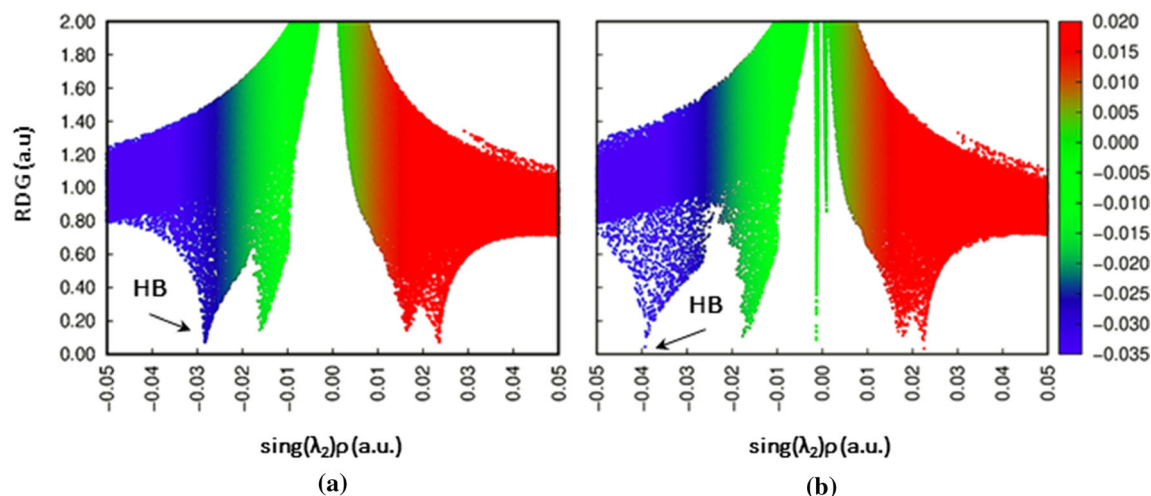


Figure 4 NCI analysis of the Cd-MOF/pNA system: bi-dimensional plot of the reduced density gradient RDG versus $\text{sign}(\lambda_2)\rho$; **a** 2D RDG plots obtained for the system in the S_0 state. **b** 2D RDG plots obtained for the system in the S_1 state.

state. Regarding this, Fengin Wang et al. [30] suggest that the feasible HB between the Cd-MOF and pNA plays an important role in the fluorescence quenching effect. However, a definitive understanding of quenching of fluorescence will come from deep insights into the optical and electronic properties of Cd-MOF and Cd-MOF/analyte systems as follows in the next section.

Optical properties of Cd-MOF

To gain a deeper understanding of the turn-off fluorescence mechanism, we explored the optical properties of Cd-MOF and 5,5'-((thiophene-2,5-dicarbonyl)bis(azanediyl))diisophthalic acid, ligand, we named as Linker, and Cd-MOF/analyte systems that were simulated via TD-DFT approach. In our previous studies, we verified the importance of considering the geometry of both the S_0 and the excited states (such as S_1 or T_1) to arrive at a robust interpretation of the sensing mechanisms [29, 28, 62, 63]. Therefore, the optical spectra, *i.e.*, absorption and emission of Cd-MOF were simulated, taking the optimized structures of the S_0 and S_1 states, respectively, as inputs in the TD-DFT calculations. Following the same procedure that was employed to compute the optical properties of the Cd-MOF/analyte system, discussion of the results is given in the next section.

The geometry of the S_0 state of Cd-MOF and linker was optimized with the aim of simulated their UV–Vis absorption spectra. In both cases, TD-DFT

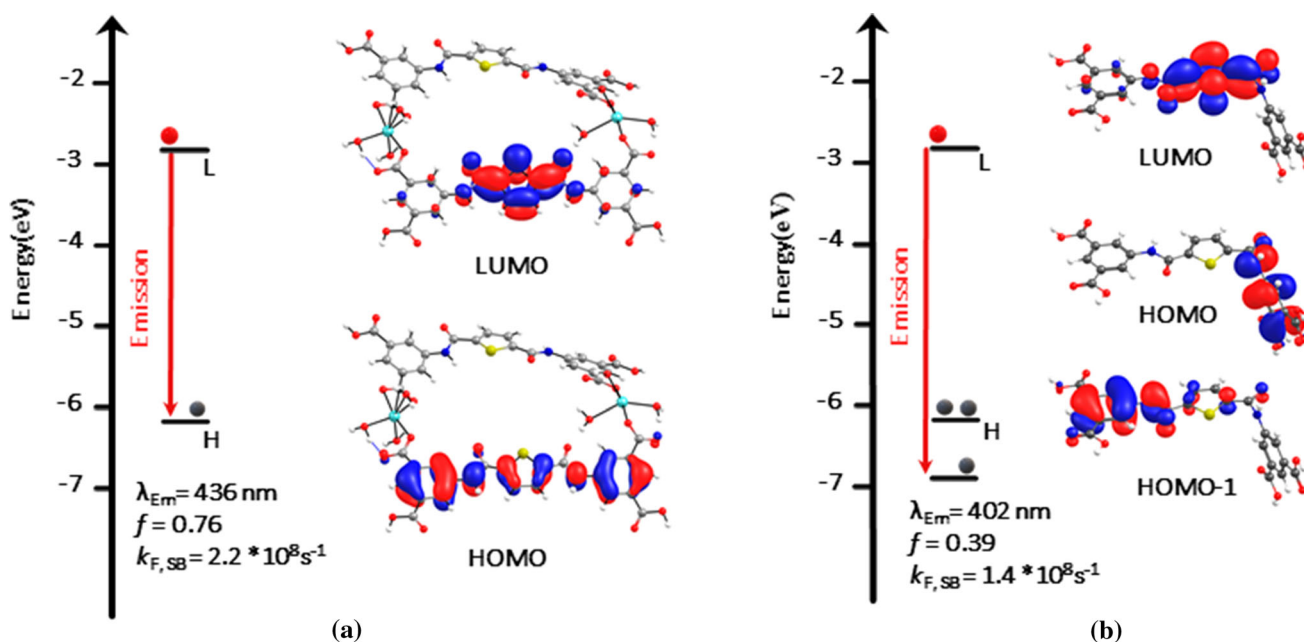
calculations reproduce the most important transitions in good agreement with the experimental report, see Table 3 and Fig. S6. From these results, it was observed that the MOs involved in the absorption band are localized along the linker. These π -type transitions that characterize the main absorption band correspond to a strong mixture of linker-centered transitions (LC), from the highest occupied MO (HOMO) to the orbital above the lowest unoccupied MO (LUMO), labeled as $(L + 1)$, and the second transition from the HOMO-1 to LUMO. The wavelength of this computed absorption band is 337 nm, which shows great concordance with the reported experimental data being 340 nm [30].

The experimental emission spectrum of Cd-MOF, excited at 340 nm, exhibits the maximum emission at 480 nm with more intensity than the linker [30]. Furthermore, this emission band was ascribed to the $\pi - \pi^*$ ligand transition, which also is a very similar emission band of the linker with a small redshift (~ 20 nm) [30]. To carry out a theoretical analysis of the chemosensors emission origin, the emission spectrum of both Cd-MOF and linker through TD-DFT calculations was simulated. The geometry of the S_1 state of both systems was used as input data to compute the excitations that constitute the emission spectra. According to the oscillator strength (f) and fluorescence rate constant $k_{F, SB}$, a high emission is evidenced in Cd-MOF in comparison with the free linker (Table S1, (a) and (b) in Fig. 5), when the linker coordinates the Cd^{2+} ions, in Cd-MOF, are almost immobilized with ordered orientation in the

Table 3 Singlet–singlet electronic transitions for absorption and emission processes of the Cd-MOF and 5,5'-((thiophene-2,5-dicarbonyl)bis(azanediy))diisophthalic acid (Linker) at B3LYP/def2-TZVPP theoretical level

System	λ_{Exp}	λ_{Theo}	f	Assignment	Active MO
<i>Absorption</i>					
Cd-MOF	340	337	1.28	π (Linker) \rightarrow π^* (Linker)	H-1 \rightarrow L
Linker	340	336	0.60	π (Linker) \rightarrow π^* (Linker)	H \rightarrow L + 1
<i>Emission</i>					
Cd-MOF	480	420	0.76	π^* (Linker) \rightarrow π (Linker)	L \rightarrow H
Linker	462	402	0.39	$\pi^* \rightarrow \pi$	H \rightarrow L

H is HOMO, L is LUMO, λ_{Theo} is a computed value, λ_{Exp} is an experimental value reported [30] and f is the oscillator strength

**Figure 5** The most relevant electronic transition involved in the emission of the Cd-MOF (a) and linker (b), where λ_{Em} is theoretical wavelength of emission (red), f is the oscillator strength and $k_{\text{F, SB}}$ is fluorescence rate constant k_{F} (Strickler–Berg).

extended network structures which restricts at least to some degree, rotation, or vibration modes of the structure. This produces an increase in the linkers rigidity, which restrict non-radiative decay, from the excited state, concerning the free linker. Thus, the coordination of the linker to the node (Cd^{2+} ions) enhances the emission in the Cd-MOF. These results do not only corroborate the experimental emission of Cd-MOF but also demonstrates that the emission comes from the linker, with an intra-linker charge-transfer character (ILCT). This emission band is associated with a $\pi \rightarrow \pi^*$ transitions, which have a composition of 97% (L \rightarrow H), see Table 3 and Fig. 5a. According to the results, the structural model based on the truncated system reproduces the optical

properties in good agreement with the experimental results reported for the studied material, which also leads us to state that the level of theory used in this study presented a good accuracy in the computation of the electronic properties.

The sensing mechanism of 4-nitraniline (pNA)

The Cd-MOF chemosensor displays changes in the fluorescence intensity after addition of some NACs, especially in the presence of pNA, which reaches above 70% of quenching efficiency upon excitation at 340 nm. To compare different optical responses, NB was also selected as it shows a smaller quenching

effect as well as NM which does not affect the luminescence of the system [30]. To gain a deeper understanding of the sensing mechanism of the pNA, TD-DFT calculations of the chemical sensor with the analyte included explicitly in the cavity of the Cd-MOF were carried out.

The calculation of the fluorescence rate constant ($k_{F,SB}$) allowed us a deeper insight into the change in the optical properties of the Cd-MOF/analyte systems. This parameter was computed using the simplified version of the Strickler–Berg equation [52, 53], where it is imperative to correct the determination of the vertical excitation energies involved both in the absorption and emission profiles. Thus, it is necessary to obtain the configurations of the first excited states (S_1 or T_1) besides the ground state, for the interacting system MOF/analyte. As shown in Table 4, the fluorescence rate constant ($k_{F,SB} = 2.6 \times 10^8 \text{ s}^{-1}$) obtained for Cd-MOF/NM is very similar to that of the Cd-MOF ($k_{F,SB} = 2.6 \times 10^8 \text{ s}^{-1}$).

It can be seen clearly that the calculated $k_{F,SB}$ are within the magnitude orders of the fluorescence decay, which agrees with the emissive response of Cd-MOF, and Cd-MOF upon addition of NM. In case of Cd-MOF/NB, the computed $k_{F,SB}$ value decreased by only one order of magnitude ($1.8 \times 10^7 \text{ s}^{-1}$) relative to $k_{F,SB}$ value of analyte-free Cd-MOF, while, $k_{F,SB}$ values for Cd-MOF/pNA are three orders of magnitude lower ($6.5 \times 10^5 \text{ s}^{-1}$) than this constant for the free Cd-MOF ($2.6 \times 10^8 \text{ s}^{-1}$). Therefore, this system has longer lifetimes in the excited state, which makes the non-radiative decay pathways more likely to act, while the f magnitude ($f = 0.003$) also manifests a low emission in Cd-MOF/pNA concerning the f found for the free Cd-MOF ($f = 0.862$). The f and the calculated $k_{F,SB}$ values are consistent with the experimental

trend in the luminescence response of Cd-MOF upon interaction with the studied analytes. It is important to note that the $k_{F,SB}$ is smaller for Cd-MOF/pNA, which shows an intermolecular HB strengthened in the S_1 state.

We also observed a relationship between the decreasing trend of $k_{F,SB}$, and the behavior of the intermolecular HB in the S_1 state, with the fluorescent response after the Cd-MOF/analyte interaction. These results agree with other previous works, which reported that the strength of intermolecular HB (host–guest), upon excitation, might induce changes in the photophysical properties. Thus, this interaction can lead to a turn-off luminescence quenching effect of the whole system [64, 65]. In this regard, several studies suggested dramatic changes in the vibrational modes, due to that intermolecular HB strengthened in the excited state. Being strengthened by this interaction, the vibronic modes associated with HB favors energy dissipation via non-radiative processes. In this context, it is also pointed out that this intermolecular HB strengthening behavior in the excited state could favor the internal conversion (IC) mechanism [59, 66, 67].

On the other hand, it is known that the photoinduced electron on the conduction band (CB) of the MOF could be transferred to a MOs of NACs with adequate energy. This PET process plays an important role in the change of luminescent properties that induced optical response in the interacting system MOF/analyte.

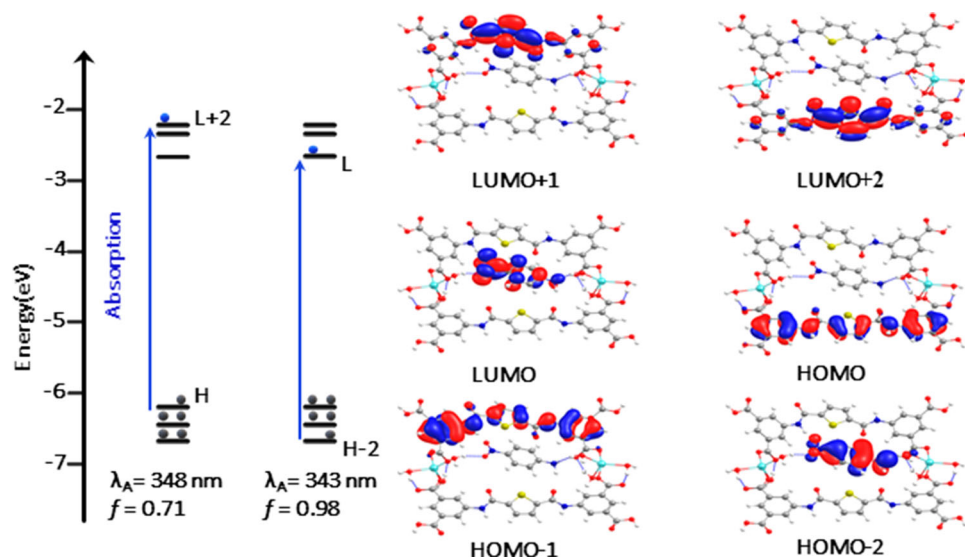
Thus, we wondered whether the electron structure of the Cd-MOF/pNA system was adequate for the PET process to occur from the Cd-MOF to the pNA. Based on the above results, we proceeded to investigate the sensing mechanism through TD-DFT calculations along with multiconfigurational ab initio methods.

The simulated UV–Vis absorption spectrum of the Cd-MOF/pNA displays two main bands regarding the strength of the oscillator (f), which are very close in energy. The first bands observed at 343 nm correspond to $\pi \rightarrow \pi^*$ transitions, that has a composition of 78% (HOMO-2 \rightarrow LUMO). According to the computations, the MOs involved in this absorption band are localized on the pNA analyte. On the other hand, the second band at 348 nm is assigned as linker-centered (LC) $\pi \rightarrow \pi^*$ transitions with a composition of 89% (HOMO \rightarrow LUMO + 2), see Fig. 6.

Table 4 Fluorescence rate constant $k_{F,SB}$ determined from the energies of vertical excitations Franck–Condon for absorption and emission, and oscillator strength (f), computed through TD-DFT, considering the solvent effect (2-Propanol, $\epsilon = 18.23$ and refraction index = 1.377)

System	$k_{F,SB} (\text{s}^{-1})$	$E_{A, \text{vert}} (\text{eV})$	$E_{F, \text{vert}} (\text{eV})$	f
Cd-MOF	2.3×10^8	3.628	2.845	0.86
Cd-MOF/NM	2.6×10^8	3.596	2.910	0.89
Cd-MOF/NB	6.5×10^7	3.592	2.882	0.06
Cd-MOF/pNA	1.8×10^5	3.565	2.549	0.003

Figure 6 Molecular orbitals involved in the electronic transitions of the two computed absorption bands for Cd-MOF/pNA, in isopropanol, where λ_A is the theoretical wavelength of absorption and f is the oscillator strength.



Recent works have suggested that fluorescence is quenched when the analyte absorbs into the excitation wavelength range of the chemosensor, by the so-called internal filter effect (IFE) [68, 69]. IFE is a process that can occur through two pathways: one requires the overlap between the absorption spectrum of the analyte (absorber) and excitation wavelength of the chemosensor (fluorophore); the another one involves the overlap of the absorption spectrum of the absorber with the emission spectrum of the fluorophore. These two pathways of attenuation of luminescence also are known as primary IFE and secondary IFE, respectively [70, 71].

Based on the simulated absorption spectra, it can be considered that there is significant competition between the pNA and Cd-MOF for the excitation energy, taking into account that the chemosensor is excited experimentally at 340 nm [30]. Therefore, to perform a deep analysis of the role of pNA and the IFE that could take place on the recognition process, we performed the following procedure. The analyte was separated from the Cd-MOF moiety in the S_0 state of the Cd-MOF/pNA. This geometry was frozen and used as input to simulate the absorption spectrum through TD-DFT calculations. From these results, it was observed an absorption band centered at 350 nm ($f = 0.41$), see Table S2, which corresponds to $\pi - \pi^*$ transition in good agreement with previous experimental works [72, 73].

Through this analysis, we confirmed the overlap between the absorption spectra of the Cd-MOF and pNA, as can be observed in Fig. S7 in the Electronic

Supplementary Material. Thus, competition between Cd-MOF and pNA by the excitation light could hinder the photoexcitation of the sensor. This result indicates that the primary IFE may contribute to the decreasing emission intensities of the Cd-MOF/pNA system.

For the Cd-MOF/NB and Cd-MOF/NM systems, the absorption spectra computed are characterized by transitions of π -type, which correspond to intra-linker-centered transitions (LC). MOs of the most important electronic transitions in the absorption bands can be seen in Fig. S8 (a) for Cd-MOF/NB and Fig. S9 (a) for Cd-MOF/NM, in the Electronic Supplementary Material. Therefore, the Cd-MOF/NB and Cd-MOF/pNA did not show any evidence of competition between chemosensor and these analytes by the excitation light, *i.e.*, the IFE is negligible for these two interacting systems. The maximum absorption wavelengths, energies, oscillator strengths, and the corresponding assignments are listed in Table S3.

PET is a photophysical phenomenon that occurs in many systems of interest as chemical sensors. Therefore, their elucidation is of great relevance to understand and propose possible mechanisms of activation/deactivation of luminescence [74].

The PET process is a transfer of electrons after photoinduced excitation between an electron-donor (D) and electron-acceptor (A) species. The chemical entities D and A can be a moiety of individual molecules or moieties of the same molecule [4]. The PET process is divided into two types, based on the

Table 5 Singlet–singlet electronic transitions, absorption and emission data, for Cd-MOF/analytes at B3LYP/def2-TZVPP theoretical level

System	λ_{Exp}	λ_{Theo}	f	Assignment	Active MO
Cd-MOF/pNA	480	486	0.003	π (pNA)* \rightarrow π (pNA)	L + 1 \rightarrow H(97%)
				π (linker)* \rightarrow π (linker)	L \rightarrow H(3%)
Cd-MOF/NB	480	430	0.064	π (NB)* \rightarrow π (linker)	L \rightarrow H(83%)
				π (linker)* \rightarrow π (linker)	L + 1 \rightarrow H(7%)
Cd-MOF/NM	480	426	0.880	π (linker)* \rightarrow π (linker)	L \rightarrow H(95%)

H is HOMO, L is LUMO, λ_{Theo} is a computed value, λ_{Exp} is an experimental value reported [30] and f is the oscillator strength

tends of the fluorophore to either gain or lose electrons, acceptor-PET and donor-PET, respectively [12, 75].

The electron-rich π -conjugated linkers increase the ability of the L-MOFs to electron transfer from the excited state to a MOs of a quencher such as the NACs [11, 15]; NACs are strong quenchers due to their high electron-deficient nature [16, 6].

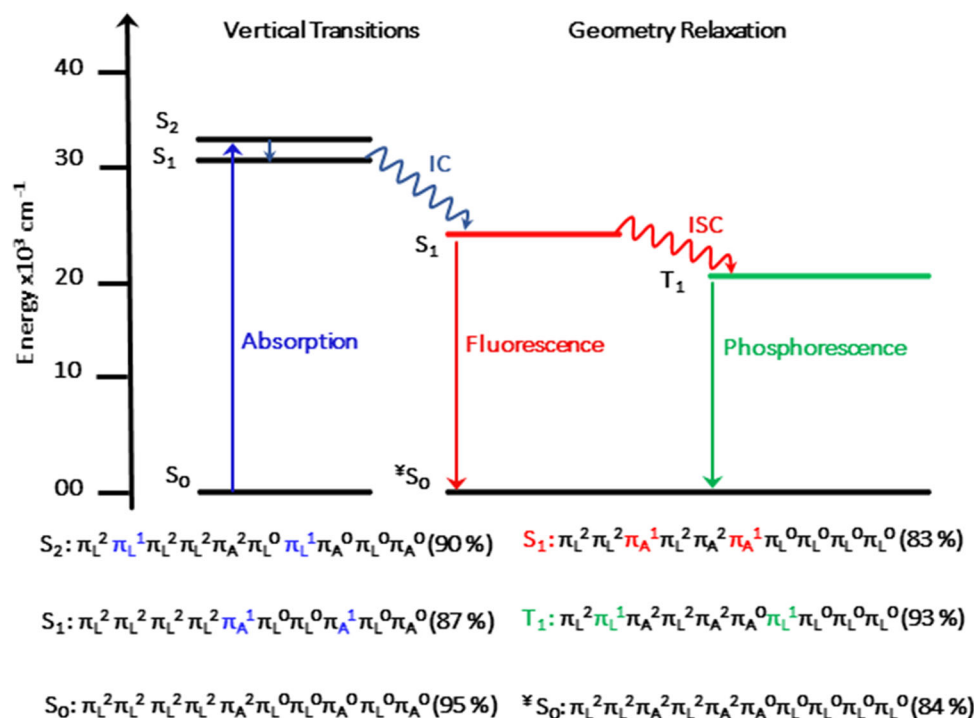
The host–guest interaction produces a mixture of MOs of sensor and analyte. Thus, the donor-PET process could take place if MOs of NACs (acceptor) appear located between the MOs involved in the emissive state of the L-MOF (donor). Upon excitation, an electron from an excited state of L-MOF is transferred to the MOs of NACs causing the non-radiative deactivation of the excited state [10, 12]. A L-MOF/analyte interaction, such as π - π stacking or hydrogen bonding, can generate stronger orbital overlap which could lead to greater PET, as has been pointed out by Lustig WP and co-workers [15].

As we reported in our recent works, the PET mechanisms in the molecular sensors based on Schiff-base can be correctly explained considering the relative energies of S_0 and S_1 electronic states of the interacting system [28, 29, 62, 63]. Based on these results, for the best of our knowledge, the optimized geometry of the S_1 electronic state of Cd-MOF/pNA was employed for the first time to compute the excitations that constitute the emission spectrum and therefore go further the sensing mechanism. In this regard, as the fluorescence involves the spin-allowed transition (transitions between states of the same spin, $S_1 \rightarrow S_0$) [76], it should be kept in mind that the radiative deactivation of the excited state arises from the lowest excited electronic state of a given multiplicity, following the Kasha's rule. So, an accurate description of the electronic structure has to be performed [27].

For Cd-MOF/pNA, the computed emission spectrum exhibits the emission band at a wavelength of 486 nm, which agrees with the experimental luminescent wavelength, $\lambda_{\text{exp}} = 480$ nm. Besides, according to the oscillator strength, this system displays a “dark” excited state, with a low emission intensity f magnitude ($f = 0.003$) concerning the f found for the free Cd-MOF ($f = 0.862$). This result is consistent with the experimental behavior turn-off luminescent sensing mechanism, of Cd-MOF upon the addition of pNA. The involved MOs responsible for this process are localized on both, the linker and the guest, *i.e.*, the pNA, see Table 5. Specifically, the LUMO (orbital π -type localized on the pNA) appears located just lower than the MOs located on the linker. According to our calculations, when pNA is confined into the Cd-MOF, it generates a mixture of MOs of both species, in the emissive state of Cd-MOF/pNA system. It is important to note here that the MOs have adequate energy to excited electrons transfers from the Cd-MOF to pNA. However, the PET process cannot be clearly explained only with this criterion of energy of the MO. Recently, we reported a theoretical procedure that allowed to confirm the existence of a state with the suitable electronic configuration and energy for the PET mechanism to occur on a molecular chemical sensor [77]. Therefore, in order to investigate whether the excited state of the interacting system Cd-MOF/pNA has the electronic configuration that favors photoinduced charge transfer, CAS(10/10)SCF/NEVPT2 calculations were performed.

This result shows that host–guest interactions produce a mixing of the Cd-MOF electronic states with those of the pNA, which are part of the active space of the interacting system Cd-MOF/pNA. At the same time, calculations showed an electronic transition that populates the S_2 state ($f = 0.366$), with 90% of the contribution of a configuration that only involves an electronic transition between MOs

Figure 7 Electronic states and most important configurations obtained from a CAS(10,10)SCF/NEVPT2 calculation considering the S_0 and S_1 state geometries. S_n and T_n represent singlet and triplet states, respectively, where IC is internal conversion and ISC is intersystem crossing. The $^{\dagger}S_0$ in the diagram refers to the configurations S_0 electronic state in the geometry of S_1 (first excited state) since fluorescence spectrum is computed as vertical transitions, as well as the simulation of phosphorescence spectrum.



located on the linker. Furthermore, the most intense electronic transition leads to a direct population of the S_1 ($f = 0.789$) state. This electronic state has an 87% contribution of the configuration which only involved MOs located on pNA, see Fig. 7a. According to our calculations, after the geometry relaxation is finally reached, the S_1 state has an 83% of the contribution of a configuration that involves a transition between MOs which are on the pNA. Besides, when the geometry relaxation of the Cd-MOF/pNA system is considered, this state appears at $24,216 \text{ cm}^{-1}$, showing a stabilization of $\sim 7772 \text{ cm}^{-1}$. These results are consistent with previous reports suggesting that the HB strengthening promotes the radiation-less depopulation of the emissive state, due to diminution of the $S_1 \rightarrow S_0$ energy gap [59, 78].

Thus, based on these results, the most probable fluorescence quenching pathway of the Cd-MOF/pNA system involves the following steps: first occurs the population of S_2 electronic state as a result of the direct electronic photoexcitation from S_0 electronic state to S_2 electronic state. After this occurs an internal conversion (IC) from the S_2 electronic state to a vibrational resonance level of the S_1 electronic state, which then deactivates to its lowest vibrational level. After the geometry relaxation finally reaches the S_1 electronic state, from which the radiative deactivation to S_0 electronic state is produced with a low oscillator

strength. Importantly, the electronic configurations of this state, evidence an emissive state located on the pNA moiety of the interacting Cd-MOF/pNA system. This suggests that in the S_1 electronic state the system has an electronic structure where the pNA-localized orbitals (acceptor) have adequate energy to accept an excited electron from the Cd-MOF (donor). Therefore, we can conclude that the mixture of states of Cd-MOF and pNA induces the S_1 state to fulfill the conditions favoring a non-radiative deactivation process. This result is consistent with the commonly accepted luminescence quenching mechanism for a MOF chemosensor selective to NACs, ascribe to photoinduced electron transfer (PET) process, from the host (MOF) to the guest (NACs) [15, 19].

In case of Cd-MOF/NB system, the computed emission spectrum displays an emission band centered at 430 nm, with a deviation of around 50 nm, which is within the error range commonly reported for TD-DFT [28, 29]. From these results, it was found that the MOs involved in the emission bands are localized both on the linker and on the NB. These transitions of π -type were assigned as $L \rightarrow H$, $\pi^*(\text{NB}) \rightarrow \pi(\text{linker})$, and $L + 1 \rightarrow H$, $\pi^*(\text{Linker}) \rightarrow \pi(\text{Linker})$, see Table 5 and Fig. S8 (b). On the other hand, the CASSCF/NEVPT2 calculations also evidence the multiconfigurational character of the electronic states of the interacting system, due to the

mixing of the Cd-MOF electronic states with those of the NB. According to the CAS(10,10)SCF/NEVPT2 calculations, the most intense electronic transition ($f = 0.389$) leads to the S_3 electronic state, that after the geometry relaxation leads to the S_1 electronic state, see Fig. S10. This electronic state has a 94% of the contribution of a configuration which involves a transition between MO located on NB. Based on the previously described outcomes, these results also evidence that the electronic structure of interacting system Cd-MOF/NB in the excited state favors the PET process between Cd-MOF and NB due to donor–acceptor interactions. Nevertheless, the oscillator strengths for this emission band only decrease one order of magnitude ($f = 0.064$ for Cd-MOF/NB) with respect to the free chemosensor ($f = 0.826$). These findings establish a strong contrast between the Cd-MOF/pNA and Cd-MOF/NB systems regarding emission intensity, based on the oscillator strength. This conclusion is consistent with two important results. First, the computed absorption spectrum for Cd-MOF/NB does not evidence that NB can compete with Cd-MOF in absorbing the excitation energy, *i.e.*, IFE process. Second, only for Cd-MOF/pNA, intermolecular HB is strengthened in the excited state, which may activate the non-radiative deactivation channels.

Overall, these results strongly argue that the PET process between the Cd-MOF and NACs is responsible for the fluorescence quenching of chemosensor. In addition, related to this remarkable fluorescent response to pNA, it is found that the strengthening of intermolecular HB in the S_1 state and IFE process, via competitive absorption of excitation energy between Cd-MOF and pNA, is responsible for the *turn-off* mechanism. To go deeper into the sensing mechanism, the simulation of the Cd-MOF/NM emission spectrum was performed, where NM is the analyte that had no evident effects on the emission intensity of Cd-MOF. The calculations show that the emission band of this system appears at 426 nm and is characterized by transitions of π -type, which correspond to linker-centered (LC) transitions, see Table 5. These electronic transitions only involve active orbitals that are localized along with the H_4L linker, see Fig. S9 (b).

Furthermore, the calculations predict that emission is due to a $\pi^* \rightarrow \pi$ transition, which has a composition of 95% (L \rightarrow H) for Cd-MOF/NM, while it is true that the host–guest interactions generate a

mixture of MOs of Cd-MOF and NM. According to the results, the electronic structure for this system shows that the MOs localized on the NM do not have adequate energy to block the radiative deactivation of Cd-MOF. It should also be noted that the MOs localized in the NM do not appear as active MOs involved in the electronic transition (absorption and emission). It is important to point out that these optical properties computed for the Cd-MOF/NM did not show significant differences between Cd-MOF without the analyte.

Ab initio Molecular Dynamics (AIMD) simulations

Finally, we exploit the ab initio molecular dynamics (AIMD) to evaluate the dynamical behavior of the intermolecular HB over time. The purpose of this analysis was to understand the dynamics of the intermolecular HB between Cd-MOF and the target NACs in this study, (*i.e.*, pNA and NB). Here, geometric criterion to describe an intermolecular interaction (O \cdots H) and (H \cdots N) of the Cd-MOF with pNA and NB, respectively, was adopted. The Cd-MOF and NACs are considered to be hydrogen-bonded if the distance R(O—H) or R(H—N) is smaller than 2.45 Å [79, 80]. The AIMD simulations show that when pNA is confined into the Cd-MOF, for all of the simulation time, four HBs facilitate intermolecular interactions between the host and the guest. Figure 8 presents the trajectories for HBs length vs. time for the Cd-MOF/pNA system. Note that three of these HBs satisfy the criterion for intermolecular HB, being the length (O—H) or (H—N) less than 2.45 Å. In the case of the Cd-MOF/NB system, the simulation indicated that there is a strong HB between the oxygen atom of the NB and the hydrogen atom of the coordinated water molecule, see Fig. S11 in the Electronic Supplementary Material. We also examined the dynamic behavior of HBs in the interacting system Cd-MOF/NACs using as input data the geometry of the S_1 state for AIMD simulations. Similar trends appear in the results obtained by considering the geometries of S_1 states for both systems, *i.e.*, Cd-MOF/pNA and Cd-MOF/NB, see Fig. S12 and S13 in the Electronic Supplementary Material. Once more, the results suggested that the analytes are encapsulated into Cd-MOF through strong intermolecular HB.

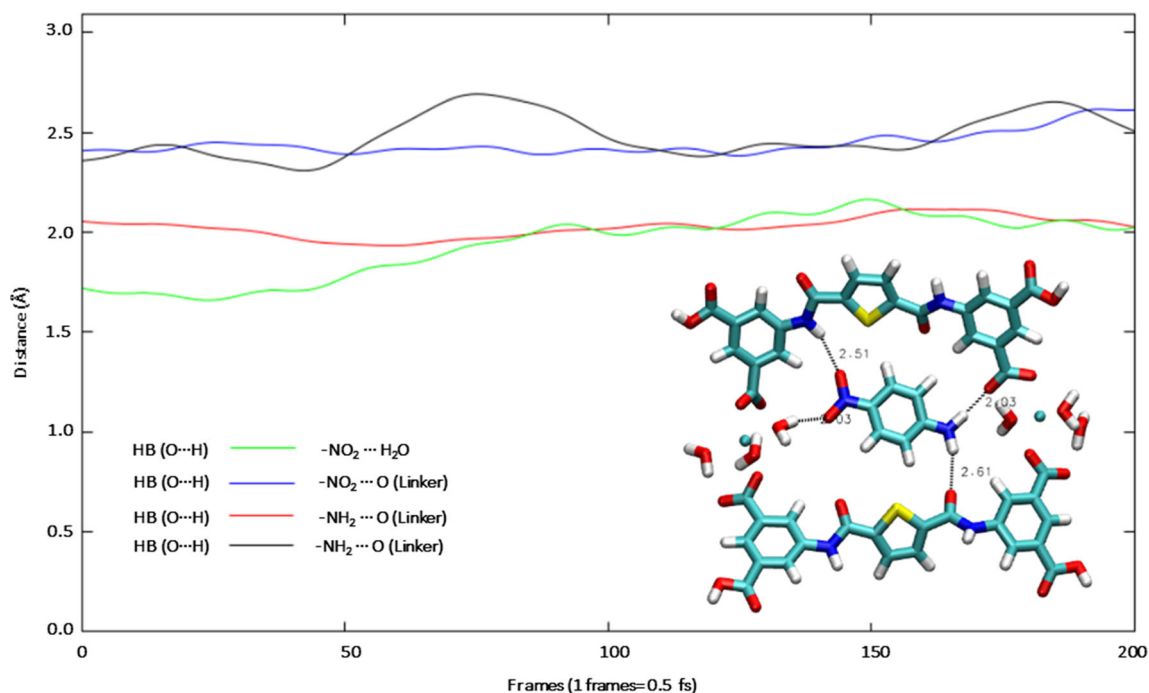


Figure 8 Time dependence of the distance intermolecular HB interactions between Cd-MOF and pNA considering the S_0 state geometries according to AIMD simulation.

Conclusions

In summary, a theoretical protocol is depicted in this work which has enabled accurately to explain the selective recognition of 4-nitroaniline (pNA) by the Cd-MOF chemosensor. The elucidation of the sensing mechanism of the target analytes by the chemosensor Cd-MOF was addressed taking into account two points (the host–guest interaction and photophysical properties): First, the study of the interacting system Cd-MOF/analyte at a rigorous theoretical level was performed, to analyze the nature of intermolecular interactions. Second, the structural and photophysical properties were evaluated, to establish the relationship between the structure of the MOF chemosensor and analyte-induced luminescence change.

In our calculations, a structural model based on the reduction of the extended system, reaching a representative fragment, $[Cd_2(H_2L)_2(H_2O)_6]$, of the Cd-MOF was proposed. The computed structural and photophysical properties obtained as result evinced that these truncated models are in excellent agreement with the reported experimental values. Besides, this truncation of the extended structures of Cd-MOF to a finite structural model does not exceed one

hundred fifteen atoms and allowed optimizing time and computational resources.

The focus of this work was to understand the selective sensing mechanism of the Cd-MOF to pNA, using the density functional theory (DFT) and time-dependent DFT (TD-DFT) calculations along with multiconfigurational ab initio methods. The photoinduced electron transfer (PET) processes were elucidated based on a detailed investigation of the electronic configuration of both the ground state and the electronically excited state of the coupled system Cd-MOF/NACs. Here, as far as our knowledge goes, this is the first work that the PET process is addressed considering the electronic configuration of interacting system MOF/analyte. TD-DFT calculations in combination with CASSCF/NEVPT2 methodology allowed us to conclude that the coupling of the linker states with those of the NACs has the adequate energy and configurations to establish an intermolecular PET from Cd-MOF to NACs. Thus, PET between Cd-MOF and pNA in the S_1 state can lock the radiative deactivation, resulting in the fluorescence quenching. Besides, we conclude that the high quenching efficiency of the Cd-MOF toward pNA is due to the strengthening of the intermolecular

interaction of the HB in the S_1 state, and the competition between of Cd-MOF and pNA for the excitation light.

In this sense, the analysis of host–guest interaction indicates that in the S_1 state, these systems have adequate electron structure to produce PET from the Cd-MOF (donor) to the NACs (acceptor). The analysis of the interacting system Cd-MOF/analyte via the Morokuma–Ziegler energy decomposition scheme and natural orbital of chemical valence (NOCV) approach was useful to confirm this statement.

These results, together with the non-covalent interactions (NCI) index, allowed us to characterize these interactions, as intermolecular HB, which is considerably strengthened in the S_1 excited state. Ab initio molecular dynamics (AIMD) simulations indicated that pNA is confined into the Cd-MOF through intermolecular HB and reveals that the HB distance is preserved during the simulation time.

Besides, this methodology allowed us to comprehend why the interaction of the NM with Cd-MOF does not lead to fluorescence quenching of this chemosensor, which is in perfect agreement with the reported experimental results. The electronic structure for this system shows that the MOs localized on the NM do not have suitable energy to block the radiative deactivation of Cd-MOF and, they do not appear as active orbitals involved in the electronic transition, both the absorption and the emission processes.

Finally, the proposed theoretical protocol allowed to explain the experimental behavior of this luminescent chemosensor. Therefore, this methodology can be used as the procedure for the accurate elucidation of the sensing mechanism proposed for other MOFs chemosensors selective to organic analytes.

Acknowledgements

The authors thank PhD Program in Molecular Physical Chemistry from University Andres Bello, a subsidy of the DAD-UNAB, FONDECYT 1180565, FONDECYT 1180017, FONDECYT 1201880, FONDECYT Iniciación Grant No 11180650 and ANID-Postdoctoral 3210271. This work was funded by ANID—Millennium Science Initiative Program—NCN17_040. ANID/FONDAP/15110019.

Supplementary Information: The online version contains supplementary material available at <http://doi.org/10.1007/s10853-021-06196-3>.

References

- [1] Ju K, Parales RE (2010) Nitroaromatic compounds, from synthesis to biodegradation. *Microbiol Mol Biol Rev* 74:250–272. <https://doi.org/10.1128/MMBR.00006-10>
- [2] Bagheri M, Masoomi MY, Morsali A, Schoedel A (2016) Two dimensional host-guest metal-organic framework sensor with high selectivity and sensitivity to picric acid. *ACS Appl Mater Interfaces* 8:21472–21479. <https://doi.org/10.1021/acami.6b06955>
- [3] Viola R, Liberatore N, Luciani D, Mengali S (2016) Quartz enhanced photoacoustic spectroscopy for detection of improvised explosive devices and precursors. *Adv Opt Technol*. <https://doi.org/10.1155/2016/5757361>
- [4] Sun X, Wang Y, Lei Y (2015) Fluorescence based explosives detection: from mechanisms to sensory materials. *Chem Soc Rev* 44:8019–8061. <https://doi.org/10.1039/x0xx00000x>
- [5] Tiwari J, Tarale P, Sivanesan S, Bafana A (2019) Environmental persistence, hazard, and mitigation challenges of nitroaromatic compounds. *Environ Sci Pollut Res* 26:28650–28667. <https://doi.org/10.1007/s11356-019-06043-8>
- [6] Gole B, Bar AK, Mukherjee PS (2014) Modification of extended open frameworks with fluorescent tags for sensing explosives: competition between size selectivity and electron deficiency. *Chem A Eur J* 20:2276–2291. <https://doi.org/10.1002/chem.201302455>
- [7] Du JL, Gao JP, Li CP et al (2017) A stable 3D Cd(II) metal-organic framework for highly sensitive detection of Cu^{2+} ions and nitroaromatic explosives. *RSC Adv* 7:49618–49625. <https://doi.org/10.1039/c7ra08977e>
- [8] Karikalan N, Kubendhiran S, Chen SM et al (2017) Electrocatalytic reduction of nitroaromatic compounds by activated graphite sheets in the presence of atmospheric oxygen molecules. *J Catal* 356:43–52. <https://doi.org/10.1016/j.jcat.2017.09.012>
- [9] Wu D, Sedgwick AC, Gunnlaugsson T et al (2017) Fluorescent chemosensors: the past, present and future. *Chem Soc Rev* 46:7105–7123
- [10] Ma X, Tao F, Zhang Y et al (2017) Detection of nitroaromatic explosives by a 3D hyperbranched σ – π conjugated polymer based on a POSS scaffold. *J Mater Chem A* 5:14343–14354. <https://doi.org/10.1039/C7TA04351A>

- [11] Hu Z, Deibert BJ, Li J (2014) Luminescent metal-organic frameworks for chemical sensing and explosive detection. *Chem Soc Rev* 43:5815–5840
- [12] Cui Y, Yue D, Huang Y et al (2019) Photo-induced electron transfer in a metal-organic framework: a new approach towards a highly sensitive luminescent probe for Fe^{3+} . *Chem Commun* 55:11231–11234. <https://doi.org/10.1039/c9cc05019a>
- [13] Hidalgo-Rosa Y, Treto-Suárez MA, Schott E et al (2020) Sensing mechanism elucidation of a chemosensor based on a metal-organic framework selective to explosive aromatic compounds. *Int J Quantum Chem*. <https://doi.org/10.1002/qua.26404>
- [14] Hidalgo-Rosa Y, Treto-Suarez MA, Schott E et al (2020) Sensing mechanism elucidation of a europium(III) metal-organic framework selective to aniline: a theoretical insight by means of multiconfigurational calculations. *J Comput Chem* 41:1956–1964. <https://doi.org/10.1002/jcc.26365>
- [15] Lustig WP, Mukherjee S, Rudd ND et al (2017) Metal-organic frameworks: functional luminescent and photonic materials for sensing applications. *Chem Soc Rev* 46:3242–3285. <https://doi.org/10.1039/C6CS00930A>
- [16] Hu Z, Deibert BJ, Li J (2014) Luminescent metal-organic frameworks for chemical sensing and explosive detection. *Chem Soc Rev* 43:5815–5840. <https://doi.org/10.1039/C4CS00010B>
- [17] Kwok RTK, Leung CWT, Lam JWY, Tang BZ (2015) Biosensing by luminogens with aggregation-induced emission characteristics. *Chem Soc Rev* 44:4228–4238. <https://doi.org/10.1039/c4cs00325j>
- [18] Cui Y, Zhang J, He H, Qian G (2018) Photonic functional metal-organic frameworks. *Chem Soc Rev* 47:5740–5785. <https://doi.org/10.1039/c7cs00879a>
- [19] Liu JQ, Luo ZD, Pan Y et al (2020) Recent developments in luminescent coordination polymers: designing strategies, sensing application and theoretical evidences. *Coord Chem Rev* 406:213145. <https://doi.org/10.1016/j.ccr.2019.213145>
- [20] Lu L, Liu W, Wang J et al (2019) Four new luminescent-organic frameworks exhibiting highly sensing of nitroaromatics: an experimental and computational insight. *Inorganica Chim Acta* 487:257–263. <https://doi.org/10.1016/j.ica.2018.12.013>
- [21] Dong B-X, Pan Y-M, Liu W-L, Teng Y-L (2017) An ultra-stable luminescent metal-organic framework for selective sensing of nitroaromatic compounds and nitroimidazole-based drug molecules. *Cryst Growth Des* 18:431–440. <https://doi.org/10.1021/acs.cgd.7b01430>
- [22] Hu Z, Qiao C, Xia Z et al (2020) A luminescent mg-metal-organic framework for sustained release of 5-fluorouracil: appropriate host-guest interaction and satisfied acid-base resistance. *ACS Appl Mater Interfaces* 12:14914–14923. <https://doi.org/10.1021/acsami.0c01198>
- [23] Osman DI, El-Sheikh SM, Sheta SM et al (2019) Nucleic acids biosensors based on metal-organic framework (MOF): Paving the way to clinical laboratory diagnosis. *Biosens Bioelectron* 141:111451. <https://doi.org/10.1016/j.bios.2019.111451>
- [24] Rowsell JLC, Yaghi OM (2005) Strategies for hydrogen storage in metal-organic frameworks. *Angew Chemie Int Ed* 44:4670–4679. <https://doi.org/10.1002/anie.200462786>
- [25] Yan D, Tang Y, Lin H, Wang D (2014) Tunable two-color luminescence and host-guest energy transfer of fluorescent chromophores encapsulated in metal-organic frameworks. *Sci Rep* 4:4337. <https://doi.org/10.1038/srep04337>
- [26] Guajardo-Maturana R, Zarate X, Claveria-Cadiz F, Schott E (2016) A silver coordination cage assembled from $[\text{Ag}_2(\text{-bis(isoxazoly)})_3]$: DFT approach to the binding forces within the host-guest interactions. *RSC Adv* 6:103346–103356. <https://doi.org/10.1039/C6RA22905K>
- [27] Kasha M (1950) Characterization of electronic transitions in complex molecules. *Discuss Faraday Soc* 9:14–19
- [28] Treto-Suárez MA, Hidalgo-Rosa Y, Schott E et al (2019) Understanding the selective-sensing mechanism of Al^{3+} cation by a chemical sensor based on schiff base: a theoretical approach. *J Phys Chem A* 123:6970–6977. <https://doi.org/10.1021/acs.jpca.9b03366>
- [29] Treto-Suárez MA, Hidalgo-Rosa Y, Schott E et al (2019) Radiative decay channel assessment to understand the sensing mechanism of a fluorescent turn-on Al^{3+} chemosensor. *Int J Quantum Chem* 120:26083. <https://doi.org/10.1002/qua.26083>
- [30] Wang F, Yu Z, Wang C et al (2017) A multifunctional metal-organic framework showing excellent fluorescence sensing and sensitization. *Sens Actuators B Chem* 239:688–695. <https://doi.org/10.1016/j.snb.2016.08.067>
- [31] Poater J, Gimferrer M, Poater A (2018) Covalent and ionic capacity of MOFs to sorb small gas molecules. *Inorg Chem* 57:6981–6990. <https://doi.org/10.1021/acs.inorgchem.8b00670>
- [32] Lee C, Yang W, Parr RG (1988) Development of the Colle-Salvetti correlation-energy formula into a functional of the electron density. *Phys Rev B* 37:785–789. <https://doi.org/10.1103/PhysRevB.37.785>
- [33] Becke AD (1993) Density-functional thermochemistry III. The role of exact exchange. *J Chem Phys* 98:5648–5652. <https://doi.org/10.1063/1.464913>
- [34] Neese F (2012) The ORCA program system, Wiley Interdiscip. *Comput Mol Sci* 2:73–78
- [35] Weigend F, Ahlrichs R (2005) Balanced basis sets of split valence, triple zeta valence and quadruple zeta valence

- quality for H to Rn: Design and assessment of accuracy. *Phys Chem Chem Phys* 7:3297–3305. <https://doi.org/10.1039/b508541a>
- [36] Sjoberg P, Politzer P (1990) Use of the electrostatic potential at the molecular surface to interpret and predict nucleophilic processes. *J Phys Chem* 94:3959–3961. <https://doi.org/10.1021/j100373a017>
- [37] Barone V, Cossi M (1998) Quantum calculation of molecular energies and energy gradients in solution by a conductor solvent model. *J Phys Chem A* 102:1995–2001. <https://doi.org/10.1021/jp9716997>
- [38] Mohan N, Suresh CH (2014) A molecular electrostatic potential analysis of hydrogen, halogen, and dihydrogen bonds. *J Phys Chem A* 118:1697–1705. <https://doi.org/10.1021/jp4115699>
- [39] Ziegler T, Rauk A (1977) Calculation of bonding energies by hartree-fock slater method. 1 transition-state method. *Theor Chim Acta* 46:1–10. <https://doi.org/10.1007/BF02401406>
- [40] Kitaura K, Morokuma K (1976) A new energy decomposition scheme for molecular interactions within the Hartree-Fock approximation. *Int J Quantum Chem* 10:325–340. <https://doi.org/10.1002/qua.560100211>
- [41] Baerends EJ, Ziegler T, Autschbach J, Bashford D, Bérces A, Bickelhaupt FM, Bo C, Boerrigter PM, Cavallo L, Chong DP et al. (2017) ADF2017, SCM, Theoretical Chemistry (Vrije Universiteit, Amsterdam, The Netherlands). <https://www.scm.com>
- [42] Mitoraj MP (2011) Bonding in ammonia borane: an analysis based on the natural orbitals for chemical valence and the extended transition state method (ETS-NOCV). *J Phys Chem A* 115:14708–14716. <https://doi.org/10.1021/jp209712s>
- [43] Grimme S, Antony J, Ehrlich S, Krieg H (2010) A consistent and accurate ab initio parametrization of density functional dispersion correction (DFT-D) for the 94 elements H-Pu. *J Chem Phys* . <https://doi.org/10.1063/1.3382344>
- [44] Boys SF, Bernardi F (1970) The calculation of small molecular interactions by the differences of separate total energies. Some procedures with reduced errors. *Mol Phys* 19:553–566. <https://doi.org/10.1080/00268977000101561>
- [45] Contreras-García J, Johnson ER, Keinan S et al (2011) NCIPLOT: a program for plotting noncovalent interaction regions. *J Chem Theory Comput* 7:625–632. <https://doi.org/10.1021/ct100641a>
- [46] Johnson ER, Keinan S, Mori-Sánchez P et al (2010) Revealing noncovalent interactions. *J Am Chem Soc* 132:6498–6506. <https://doi.org/10.1021/ja100936w>
- [47] Lu T, Chen F (2012) Multiwfn: a multifunctional wavefunction analyzer. *J Comput Chem* 33:580–592. <https://doi.org/10.1002/jcc.22885>
- [48] Humphrey W, Dalke A, Schulten K (1996) VMD: visual molecular dynamics. *J Mol Graph* 14:33–38
- [49] Phillips JC, Braun R, Wang W, Gumbart J, Tajkhorshid E, Villa E, Chipot C, Skeel RD, Kale L, Schulten K (2005) Scalable molecular dynamics with NAMD. *J Comput Chem* 26:1781–1802. <https://doi.org/10.1002/jcc.20289>
- [50] Treto-Suárez MA, Tapia J, Hidalgo-Rosa Y et al (2020) New sensitive and selective chemical sensors for Ni²⁺ and Cu²⁺ Ions: insights into the sensing mechanism through DFT methods. *J Phys Chem A* 124:6493–6503. <https://doi.org/10.1021/acs.jpca.0c03834>
- [51] Zhang X, Chi L, Ji S et al (2009) Rational design of d-PeT phenylethynylated-carbazole monoboronic acid fluorescent sensors for the selective detection of α -hydroxyl carboxylic acids and monosaccharides. *J Am Chem Soc* 131:17452–17463. <https://doi.org/10.1021/ja9060646>
- [52] Shi J, Izquierdo MA, Oh S et al (2019) Inverted energy gap law for the nonradiative decay in fluorescent floppy molecules: larger fluorescence quantum yields for smaller energy gaps. *Org Chem Front* 6:1948–1954. <https://doi.org/10.1039/c9qo00259f>
- [53] Shi J, Aguilar Suarez LE, Yoon SJ et al (2017) Solid state luminescence enhancement in π -conjugated materials: unraveling the mechanism beyond the framework of AIE/AIEE. *J Phys Chem C* 121:23166–23183. <https://doi.org/10.1021/acs.jpcc.7b08060>
- [54] Roos BO, Taylor PR, Sigbahn PEM (1980) A complete active space SCF method (CASSCF) using a density matrix formulated super-CI approach. *Chem Phys* 48:157–173. [https://doi.org/10.1016/0301-0104\(80\)80045-0](https://doi.org/10.1016/0301-0104(80)80045-0)
- [55] Angeli C, Cimraglia R, Evangelisti S et al (2001) Introduction of n-electron valence states for multireference perturbation theory. *J Chem Phys* 114:10252. <https://doi.org/10.1063/1.1361246>
- [56] Bentzien J, Muller RP, Floria J, Warshel A (1998) Hybrid ab initio quantum mechanics / molecular mechanics calculations of free energy surfaces for enzymatic reactions: the nucleophilic attack in subtilisin. *J Phys Chem B* 102:2293–2301. <https://doi.org/10.1021/jp973480y>
- [57] Carloni P, Rothlisberger U, Parrinello M (2002) The role and perspective of Ab initio molecular dynamics in the study of biological systems. *Acc Chem Res* 35:455–464. <https://doi.org/10.1021/ar010018u>
- [58] Biczók L, Bérces T, Linschitz H (1997) Quenching processes in hydrogen-bonded pairs: interactions of excited fluorenone with alcohols and phenols. *J Am Chem Soc* 119:11071–11077. <https://doi.org/10.1021/ja972071c>
- [59] Inoue H, Hida M, Nakashima N, Yoshihara K (1982) Picosecond fluorescence lifetimes of anthraquinone derivatives. Radiationless deactivation via intra- and

- intermolecular hydrogen bonds. *J Phys Chem* 86:3184–3188. <https://doi.org/10.1021/j100213a024>
- [60] Politzer P, Murray JS (1991) Molecular electrostatic potentials and chemical reactivity. *Rev Comput Chem*. <https://doi.org/10.1002/chin.200427290>
- [61] Mitoraj MP, Michalak A (2013) Theoretical description of halogen bonding—An insight based on the natural orbitals for chemical valence combined with the extended-transition-state method (ETS-NOCV). *J Mol Model* 19:4681–4688. <https://doi.org/10.1007/s00894-012-1474-4>
- [62] Berrones-Reyes J, Muñoz-Flores BM, Gómez-Treviño A et al (2019) Novel fluorescent schiff bases as Al³⁺ sensors with high selectivity and sensitivity, and their bioimaging applications. *Mater Chem Phys* 233:89–101. <https://doi.org/10.1016/j.matchemphys.2019.05.035>
- [63] Berrones-Reyes JC, Muñoz-Flores BM, Cantón-Díaz AM et al (2019) Quantum chemical elucidation of the turn-on luminescence mechanism in two new Schiff bases as selective chemosensors of Zn²⁺: synthesis, theory and bioimaging applications. *RSC Adv* 9:30778–30789. <https://doi.org/10.1039/c9ra05010h>
- [64] Zhao Z, Song X, Liu L et al (2018) A recognition mechanism study: Luminescent metal-organic framework for the detection of nitro-explosives. *J Mol Graph Model* 80:132–137. <https://doi.org/10.1016/j.jmgm.2017.12.024>
- [65] Wang P, Song X, Zhao Z et al (2016) Role of the electronic excited-state hydrogen bonding in the nitro-explosives detection by [Zn₂(oba)₂(bpy)]. *Chem Phys Lett* 661:257–262. <https://doi.org/10.1016/j.cplett.2016.06.085>
- [66] Zhao G-J, Han K-L (2007) Ultrafast hydrogen bond strengthening of the photoexcited fluorenone in alcohols for facilitating the fluorescence quenching[†]. *J Phys Chem A* 111:9218–9223. <https://doi.org/10.1021/jp0719659>
- [67] Flom SR, Barbara PF (1985) Proton transfer and hydrogen bonding in the internal conversion of S1 anthraquinones. *J Phys Chem* 89:4489–4494. <https://doi.org/10.1021/j100267a017>
- [68] Fan L, Wang F, Zhao D et al (2020) Two cadmium(II) coordination polymers as multi-functional luminescent sensors for the detection of Cr(VI) anions, dichloronitroaniline pesticide, and nitrofurant antibiotic in aqueous media. *Spectrochim Acta - Part A Mol Biomol Spectrosc* 239:118467. <https://doi.org/10.1016/j.saa.2020.118467>
- [69] Fan L, Wang F, Zhao D et al (2020) A self-penetrating and chemically stable zinc (ii)-organic framework as multi-responsive chemo-sensor to detect pesticide and antibiotics in water. *Appl Organomet Chem*. <https://doi.org/10.1002/aoc.5960>
- [70] Chen S, Yu YL, Wang JH (2018) Inner filter effect-based fluorescent sensing systems: a review. *Anal Chim Acta* 999:13–26. <https://doi.org/10.1016/j.aca.2017.10.026>
- [71] Panigrahi SK, Mishra AK (2019) Inner filter effect in fluorescence spectroscopy: as a problem and as a solution. *J Photochem Photobiol C Photochem Rev* 41:100318. <https://doi.org/10.1016/j.jphotochemrev.2019.100318>
- [72] Kozich V, Werncke W, Dreyer J et al (2002) Vibrational excitation and energy redistribution after ultrafast internal conversion in 4-nitroaniline. *J Chem Phys* 117:719–726. <https://doi.org/10.1063/1.1482698>
- [73] Kovalenko SA, Farztdinov VM, Schanz R, et al (2000) Femtosecond relaxation of photoexcited p-nitroaniline in water: solvation internal conversion and cooling. *Conference Quantum Electron Laser Sci - Tech Dig Ser* 195
- [74] Natali M, Campagna S, Scandola F (2014) Photoinduced electron transfer across molecular bridges: electron- and hole-transfer superexchange pathways. *Chem Soc Rev* 43:4005–4018. <https://doi.org/10.1039/C3CS60463B>
- [75] Chen Y, Tsao K, Keillor JW (2015) Fluorogenic protein labelling: a review of photophysical quench mechanisms and principles of fluorogen design. *Can J Chem* 93:389–398. <https://doi.org/10.1139/cjc-2014-0405>
- [76] Feng Y, Cheng J, Zhou L et al (2012) Ratiometric optical oxygen sensing: a review in respect of material design. *Analyst* 137:4885. <https://doi.org/10.1039/c2an35907c>
- [77] Treto-Suárez MA, Hidalgo-Rosa Y, Schott E et al (2020) Fluorescence turn-on and turn-off mechanisms of a dual-selective chemosensor of Bi³⁺ and Ph changes: insights from a theoretical perspective. *Dye Pigment*. <https://doi.org/10.1016/j.dyepig.2020.108934>
- [78] Liu YH, Zhao GJ, Li GY, Han KL (2010) Fluorescence quenching phenomena facilitated by excited-state hydrogen bond strengthening for fluorenone derivatives in alcohols. *J Photochem Photobiol A Chem* 209:181–185. <https://doi.org/10.1016/j.jphotochem.2009.11.012>
- [79] Chandra A (2003) Dynamical behavior of anion–water and water–water hydrogen bonds in aqueous electrolyte solutions: a molecular dynamics study. *J Phys Chem B* 107:3899–3906. <https://doi.org/10.1021/jp022147d>
- [80] Naberukhin YI, Voloshin VP (2009) Distributions of hydrogen bond lifetimes in instantaneous and inherent structures of water. *Zeitschrift fur Phys Chemie* 223:1119–1131. <https://doi.org/10.1524/zpch.2009.6062>

Publisher's Note Springer Nature remains neutral with regard to jurisdictional claims in published maps and institutional affiliations.